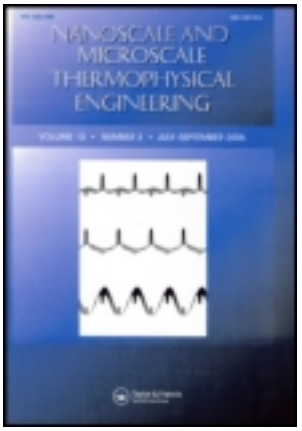

Nanoscale and Microscale Thermophysical Engineering
Publication details, including instructions for authors and subscription information:
http://www.tandfonline.com/loi/umte20

Phonon Conduction in Periodically Porous Silicon Nanobridges

Amy M. Marconnet [a], Takashi Kodama [a], Mehdi Asheghi [a] & Kenneth E. Goodson [a]
[a] Department of Mechanical Engineering, Stanford University, Stanford, California
Version of record first published: 04 Dec 2012.

To cite this article: Amy M. Marconnet , Takashi Kodama , Mehdi Asheghi & Kenneth E. Goodson (2012): Phonon Conduction in Periodically Porous Silicon Nanobridges, Nanoscale and Microscale Thermophysical Engineering, 16:4, 199-219

To link to this article: http://dx.doi.org/10.1080/15567265.2012.732195

Nanoscale and Microscale Thermophysical Engineering, 16: 199–219, 2012

ISSN: 1556-7265 print / 1556-7273 online
DOI: 10.1080/15567265.2012.732195

PHONON CONDUCTION IN PERIODICALLY POROUS SILICON NANOBRIDGES

Amy M. Marconnet, Takashi Kodama, Mehdi Asheghi, and Kenneth E. Goodson

Department of Mechanical Engineering, Stanford University, Stanford, California

Thermal conduction in periodically porous nanostructures is strongly influenced by phonon boundary scattering, although the precise magnitude of this effect remains open to investigation. This work attempts to clarify the impact of phonon-boundary scattering at room temperature using electrothermal measurements and modeling. Silicon nanobeams, prepared using electron beam lithography, were coated with a thin palladium overlayer, which serves as both a heater and thermometer for the measurement. The thermal conductivity along the length of the silicon nanobeams was measured using a steady-state Joule heating technique. The thermal conductivities of the porous nanobeams were reduced to as low as 3% of the value for bulk silicon. A Callaway-Holland model for the thermal conductivity was adapted to investigate the relative impact of boundary scattering, pore scattering, and phonon bandgap effects. Both the experimental data and the modeling showed a reduction in thermal conductivity with increasing pore diameter, although the experimentally measured value was up to an order of magnitude lower than that predicted by the model.

KEY WORDS: thermal conductivity, porous silicon, phononic crystals

INTRODUCTION

Nanostructured materials offer the possibility of thermal conductivity extremes. At one extreme, the thermal conductivities of carbon nanotubes and graphene can exceed those of metals [1]. On the other, the introduction of nanoscale boundaries such as those of nanowires [2] and grains [3] can significantly reduce the thermal conductivity. Reducing the thermal conductivity without significantly impacting the electrical conductivity and Seebeck coefficient improves the thermoelectric figure of merit. In thin silicon films, the thermal conductivity can be reduced through the introduction of nanoscale or microscale periodic pore structures, sometimes referred to as *phononic crystals* [4–6]. This name makes an analogy with photonic crystal cavities, such as those in silicon [7] and other material systems [8], for which careful design of pore structures leads to a photonic bandgap associated with wavelengths comparable to the periodic length scales of the cavity. The

Manuscript received 19 January 2012; accepted 12 September 2012.

The authors gratefully acknowledge financial support from MARCO Interconnect Focus Center, the National Science Foundation Graduate Research Fellowship program, and the Stanford Graduate Fellowship program.

Address correspondence to Amy M. Marconnet, Department of Mechanical Engineering, Stanford University, Building 530, Room 224, 440 Escondido Mall, Stanford, CA 94305. E-mail: tennocrama@gmail.com

NOMENCLATURE

A	fitting constant for the impurity scattering term, $A = 1.32 \times 10^{-45}$ s^3
$\boldsymbol{A}$	matrix used in electrothermal model
A_c	cross-sectional area
AR	aspect ratio, AR $= W/H$
B	fitting constant for the Umklapp scattering term, $B = 1.4 \times 10^{-19}$ S/K
$\boldsymbol{B}$	vector used in electrothermal model
C	fitting constant for the Umklapp scattering term, $C = 152$ K
C_j	heat capacity per phonon mode
D	pore diameter
E	fitting constant for the bulk scattering term, $E = 2.3 \times 10^{-3}$ m
F	thermal conductivity reduction function
f_{ph}	frequency of phonons impacted by a phononic crystal cavity
H	thickness
h	Planck's constant
I	current
k	thermal conductivity
k_b	Boltzmann constant
L	beam length
L_e	length of the nonporous region of the nanoladders
N_h	number of holes in the nanoladder
N_p	number of phonon paths
n	index in summation
O	phonon point of origin
$\overline{OP}$	distance phonon travels between origin and nanobeam boundary
$\overline{OR}$	distance phonon travels between origin and pore boundary
P	limiting dimension
p	specularity parameter
q	phonon wave vector
q_{gen}	heat generation rate
q_{in}	rate of heat transfer into the control volume
q_{out}	rate of heat transfer out of the control volume
R	electrical resistance
S	pore spacing (pitch)
T	temperature
T_o	reference temperature
U	nanowire/nanobeam cross-sectional area
V	voltage
v	phonon velocity
v_{avg}	average speed of sound
W	beam width
x	distance along length of nanoladder
Δx	length of the differential element in the x-direction

Greek Symbols

α	temperature coefficient of resistivity
Γ	phonon transmission function
γ	$\gamma^2 I^2 R_0 \alpha / [WL(k_m H_m + k_s H_s)]$
δ	reduced thickness, $\delta = H/E$
θ	polar angle
$\hbar$	$h/2\pi$
Λ	phonon mean free path
ρ	electrical resistivity
σ	electrical conductivity
τ	phonon relaxation time
φ	azimuthal angle
ω	phonon angular frequency

Subscripts

0	selected mean free path
B	bulk
boundary	due to boundary scattering
bulk	due to scattering mechanisms in bulk silicon
e	of the nonporous beam ends
i	discretization index in numerical model
impurity	due to scattering on impurities
j	phonon branch index
m	of the metal layer
o	at the reference temperature
p	of the porous region of the beam
pores	due to scattering on the pores
r	reduced
s	of the silicon layer
Umklapp	due to Umklapp scattering processes

demonstration of a phononic crystal influencing heat conduction is extremely challenging due to the very small dominant phonon wavelengths (<5 nm at room temperature [9]), as well as the significant variation in the wavelengths of thermal phonons about the dominant value. Several groups are studying phononic crystals and are investigating modifications to the phonon dispersion relationship through the introduction of periodic pore structures [10–14]. These pores introduce a high density of interfaces that impede phonon conduction due to higher scattering rates. It is important to isolate these classical ballistic scattering effects, which are themselves challenging to precisely quantify, from any interpretation considering a modification of the phonon band structure.

Though the thermal conductivity of two-dimensional periodically porous materials has been studied across a range of dimensions [6, 15], thermal transport in nanobridges with single-row pores (henceforth called *nanoladders*), which have been used as photonic crystal cavities [16], merits more attention. These structures present an interesting opportunity to examine the impact of pore geometry and boundary scattering on thermal transport. In this article, we discuss thermal transport in silicon nanoladders both from an experimental and analytical viewpoint. We use a steady-state four-probe electrothermal measurement technique to measure the thermal conductivity and a Callaway-Holland-type model to further investigate effects of pore and boundary scattering.

ELECTROTHERMAL MEASUREMENT

The thermal conductivity of the nanoladders is characterized using a four-probe, steady-state electrothermal measurement technique, similar to that of Liu and Asheghi [17, 18]. A metal film deposited on the silicon nanostructure serves as a heater and thermometer for the measurement of thermal properties. The fabrication process starts from a silicon-on-insulator wafer and requires only one lithography step to form both the nanoladder and the four electrical contact pads. The silicon device layer is thinned to ~200 nm using oxidation and wet etching prior to electron beam lithography. The nanoladder and probe pads are patterned using electron beam lithography and the silicon is dry etched. Next, the SiO_2 layer beneath the silicon nanoladder device is removed using a 6:1 solution of buffered oxide etchant for ~15 min to completely suspend the nanoladder device. Because the oxide etchant is isotropic, in addition to the nanoladder itself, the paths to the current and voltage probe pads are suspended. Finally, a 40-nm film of palladium is deposited on the suspended device using electron beam evaporation (Innotec ES26C; Innotec Group, Simi Valley, CA). A scanning electron micrograph (SEM) of the device design is shown in Figure 1a, and the suspended region is indicated by the dashed lines. A schematic of the device cross section is shown in Figure 1b. The palladium thickness H_m is calculated from the deposition rate and time. The pore diameter D, pitch S, beam width W, beam length L, and silicon thickness H are measured from SEMs.

Electrical current is passed through the palladium film and the temperature T increases due to Joule heating, while the electrical conductivity σ decreases proportional to the temperature. To illustrate the effect of Joule heating, Figure 1c shows the results of a numerical model of the temperature rise and associated electrical conductivity reduction for the nonporous nanobeam at the maximum applied current. In order to minimize heat loss to ambient, the experiments were carried out in a vacuum (≤20 mTorr). COMSOL (Burlington, MA) models of the nanobeam measurement structure showed that the radiation losses were negligible for all applied current levels. The current was increased in steps and the electrical resistance R of the nanoladder was measured through the measured

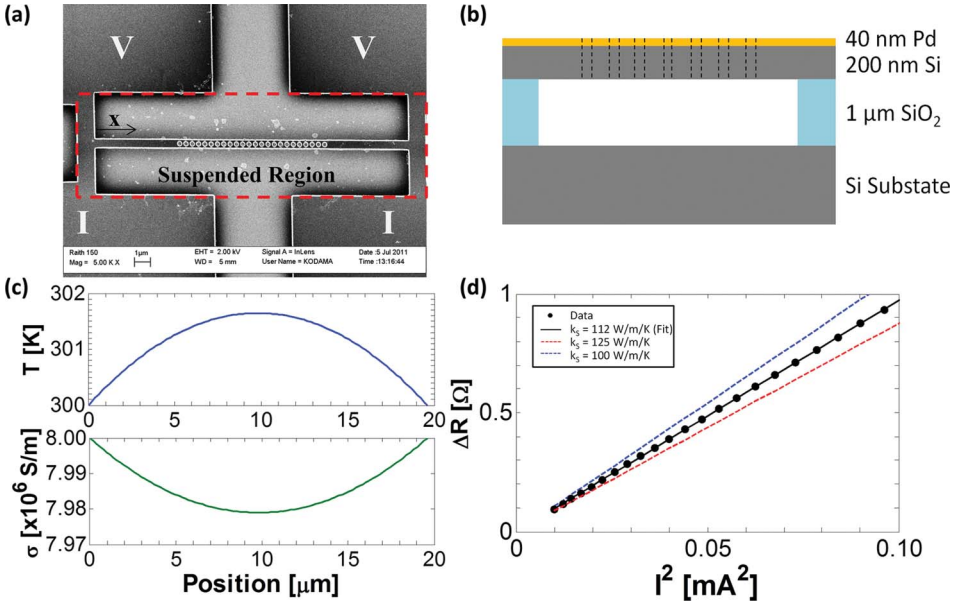

Figure 1 (a) SEM of a nanoladder measurement device. The nanoladder is connected to four electrical probe pads (two for applying current [marked I] and two for measuring voltage [marked V]). The dashed rectangle approximately marks the extent of the suspended region. (b) Cross section of a nanoladder measurement device. The nanoladder is fabricated using electron beam lithography from a silicon-on-insulator wafer with 200-nm device layer and a 1-μm-thick oxide layer. Forty nanometers of palladium is deposited on the devices and serves as both a heater and a thermometer in the system. (c) Calculated temperature profile along the nanobeam and corresponding electrical conductivity for the beam without holes at 300 mA applied current. For each current level, a numerical electrothermal model is used to calculate the temperature profile along the nanoladder and extract the increase in electrical resistance. (d) Comparison of measured and predicted increase in electrical resistance as a function of the square of the applied current for a silicon nanobeam without holes. The measured increase in resistance depends strongly on the thermal conductivity of the silicon layer as indicated by the best fit line with $k_S = 112$ W m^{-1} K^{-1} (solid black line) compared to $k_S = 100$ W m^{-1} K^{-1} (dashed blue line) and $k_S = 125$ W m^{-1} K^{-1} (dashed red line) (color figure available online).

voltage V across the nanoladder. Figure 1d shows an example plot of the change in resistance as a function of the square of current.

The temperature coefficient of resistance α and the electrical resistivity ρ_o of the palladium film were determined for each nanoladder by measuring the resistance at low current; that is, in the linear region of the I-V curves. The low current electrical resistance data at temperatures between 300 and 320 K were fit to $R(T) = R_o(1 + \alpha(T - T_o))$, where R_o is the electrical resistance at the reference temperature T_o. The temperature coefficient of resistance was $\alpha = 0.0017$ K^{-1}. The electrical resistivity of the palladium layer on the nanoladders at 300 K was calculated from the electrical resistance and geometry. For the nonporous nanobeam and the nanoladders with 110- and 210-nm-diameter pores, the electrical resistivity of the 40-nm-thick palladium was $\rho_o = 28$ μΩ·m and for the nanoladder with 280-nm-diameter pores, $\rho_o = 40$ μΩ·m. Using the Wiedemann-Franz law, the thermal conductivity of the palladium layer was estimated to be 26 and 18 W m^{-1} K^{-1} for the small- and large-diameter pore cases, respectively. The estimated thermal conductivity and electrical parameters were close to the value measured independently for solid palladium nanobeams of the same thickness and similar beam widths [19].

A combined electrical and thermal model was used to fit the data and extract the silicon nanoladder thermal conductivity. Heat transfer was assumed to be one-dimensional along the length of the nanoladder (x-direction), and thermal conduction in both the silicon and palladium films was included. In the case of a uniform cross-section beam with constant thermal conductivity, the temperature profile along the beam can be computed analytically from [18]:

$$T(x) = T_o - \frac{1}{\alpha}\left(1 - \frac{\cos \gamma x}{\cos(\gamma L/2)}\right), \tag{1}$$

where $\gamma^2 = {I^2 R_o \alpha}/{[WL\,(k_m H_m + k_s H)]}$, and k_m and k_s are the thermal conductivities of the palladium and silicon layers, respectively. Using Eq. (1), the average electrical resistance of the beam as a function of applied current can be determined [18]:

$$R = R_o\left[\frac{2}{\gamma L}\tan\left(\frac{\gamma L}{2}\right)\right]. \tag{2}$$

Given the palladium thermal conductivity, the thermal conductivity of the silicon nanobeam can be extracted by fitting the data with this equation. However, this model is only valid for beams with uniform cross sections (i.e., beams without holes).

For the nanoladders, we developed a numerical model to calculate the temperature profile and electrical resistance allowing for spatially varying cross-sectional area, different silicon thermal conductivies for the porous ($\sim$10 μm at center of beam) and nonporous ($\sim$5 μm at each end of the beam) regions, and temperature-dependent palladium electrical resistivity. This model allows direct extraction of the solid silicon thermal conductivity, as opposed to an effective conductivity of the porous solid that would be obtained if the varying cross section were neglected. Using the finite difference method, the temperature profile along the nanoladder and the increase in electrical resistance at each measured current level were calculated. The silicon nanoladder thermal conductivity was extracted by fitting the model to the resistance versus current data using a nonlinear least-squares fitting routine. Because the ends of the beams had no holes, the ends were assumed to have the thermal conductivity extracted for the beam without holes. Thus, only the silicon thermal conductivity in the center portion of the beam was varied in the fitting routine. Additional details of the model can be found in Appendix A.

The thermal conductivity of one nonporous nanobeam and three nanoladders (570 nm wide, 18.8 μm long) with different pore diameters (110, 210, or 280 nm) was measured. Each nanoladder had 24 pores, spaced by 385 nm. The silicon nanobeam layer was 196 nm thick and the palladium film was 40 nm thick. All measured thermal conductivities were reduced from the thermal conductivity of bulk silicon. Specifically, the extracted thermal conductivities of the nanoladders were 54, 3.7, and 3.4 W m^{-1} K^{-1} for the nanoladders with 110-, 210-, and 280-nm-diameter pores, respectively (see Figure 2). For comparison, the thermal conductivity data from Kim et al. [20] (in-plane) and Hopkins et al. [5] (out-of-plane) for two-dimensional phononic crystal films with pore spacings ranging from 500 to 800 nm are included in Figure 2. Note that the out-of-plane thermal conductivities shown in Figure 2 from Hopkins et al. [5] were modified by the solid fill fraction, not the Eucken factor.

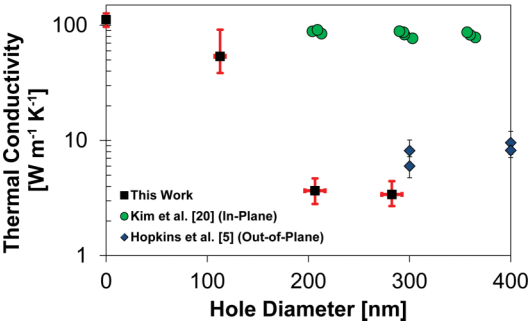

Figure 2 Silicon nanoladder thermal conductivity. For the 200-nm-thick nanoladders, the pores are spaced by 385. For the nanoladders with 110-nm-diameter pores, the uncertainty in the thermal conductivity of the nonporous regions of the beam dominates the uncertainty in thermal conductivity of the porous region. For the larger diameter pore cases, the uncertainty is largely due to uncertainty in the measured value of the pore diameter. For comparison, the thermal conductivity data for two-dimensional phononic crystals with pore spacings ranging from 500 to 800 nm fabricated from 500-nm-thick Si films from Kim et al. [20] (circles, in-plane conductivity) and Hopkins et al. [5] (diamonds, out-of-plane conductivity) (color figure available online).

Surface roughness plays an important role in the scattering of phonons in silicon nanostructures. Using molecular and lattice dynamics, He et al. [21] showed that the disorder at the surface of ∼2- to 10-nm-diameter pores in a periodically porous silicon film reduces the thermal conductivity compared to smooth pores. Hochbaum et al. [22] experimentally found that the thermal conductivity of rough silicon nanowires was significantly lower than that of smooth nanowires. As evident from SEMs (not shown), the surface roughness of these nanoladder devices was quite large and could contribute to the extremely low thermal conductivity. Additionally, past studies [23] have shown that reactive ion etching can cause defective regions near the etched surfaces. These defective regions, in addition to the surface roughness, may contribute to the low experimentally observed thermal conductivity.

Uncertainty in the thermal conductivity of the nonporous region contributes to uncertainty in the thermal conductivity of the porous region. It has the largest effect for the smallest diameter pore case, where the thermal conductivity is closest to that of the nonporous nanobeam. If the thermal conductivity of the nonporous region is reduced by 10%, the thermal conductivity extracted for the porous region in the 100-nm-diameter case increases from 54 to 92 W m^{-1} K^{-1}. In contrast, for the largest diameter holes (280 nm), a 10% reduction in the thermal conductivity of the nonporous region only increases the extracted thermal conductivity from 3.4 to 3.7 W m^{-1} K^{-1}. For the nanoladders with larger holes (210 and 280 nm diameters), the temperature rise in the nanoladder is dominated by the temperature rise in the porous region of the beam. However, for the smaller diameter case (110 nm), the temperature rise in the nonporous region of the beam is predicted to be approximately half of the total temperature rise and, thus, 10% changes in the thermal conductivity of the nonporous region lead to significant changes in the fitted thermal conductivity of the porous region of the beam. A fixed upper limit on the extracted value of the thermal conductivity of the nanoladders can be found by assuming that the porous and nonporous regions have the same thermal conductivity. In this case, the extracted average nanoladder thermal conductivities are ∼100, 30, and 25 W m^{-1} K^{-1} for the nanoladders with 110-, 210-, and 280-nm diameter pores, respectively. In future

work, the nonporous end region of the nanoladder should be eliminated for the geometry to reduce the uncertainty in the nanoladder measurements.

The geometry of the nanoladders was measured from SEMs and the surface roughness of the edges of the nanoladder and pore boundaries was evident. Edge effects in the SEM image led to some uncertainty as to the exact location of the edge of the silicon. Additionally, some of the pores were not quite perfectly circular and there was a slight variation between pore diameters within each nanoladder. The uncertainty in the pore diameter (± 10 nm) dominated the uncertainty in thermal conductivity for the samples with 210- and 280-nm pores.

Because the extracted values of thermal conductivity for the large-pore-diameter nanoladders were quite low, fitting the data with a one-dimensional heat transfer model may actually underestimate the thermal conductivity. To estimate the impact of the one-dimensional heat transfer assumption, the magnitude of the extracted thermal conductivity was confirmed with two additional models. The first assumed that "rungs" of the nanoladder do not contribute to heat transfer and that the sides of the nanoladder act as two parallel nanobeams of width $(W - D)/2$. In this case, the extracted thermal conductivities of the 210- and 280-nm pore diameter nanoladders roughly doubled to 6.4 and 7.3 W m^{-1} K^{-1}, respectively. In the second, a fully three-dimensional COMSOL finite element model was used to fit the data for the 280-nm pore diameter nanoladder. The COMSOL model considered the same geometry, boundary conditions, and material properties as explained in Appendix A for the one-dimensional numerical model. The electrical and thermal solvers were coupled through Joule heating and temperature-dependent electrical conductivity in the palladium layer, and only thermal transport was considered in the silicon nanobeam. Using this three-dimensional model, the thermal conductivity was estimated to be 4.9 W m^{-1} K^{-1}, a 45% increase in the value from the one-dimensional heat transfer assumption.

As previously mentioned, the crossbars between the probe pads and the nanoladder were also suspended due to the isotropic etching of the SiO_2. However, they were designed with a larger cross section than the nanobeam itself to ensure minimal thermal resistance between the end of the nanoladder and the substrate. From a simple thermal resistance point of view, the thermal resistance of the crossbars was small in comparison to the total thermal resistance of the structure, so the temperature rise at the ends of the nanobeam was expected to be small. However, there was some heat generation in the current path portion of the crossbar, so a COMSOL model including the crossbars was developed to confirm the impact of this geometry. For the 280-nm pore diameter nanoladders, the extracted value of thermal conductivity did not change when the crossbeams were included in the simulation and the temperature rise at the ends of the nanobeam never exceeded 1% of the maximum temperature rise in the nanoladder.

MODELING THE THERMAL CONDUCTIVITY OF SILICON NANOLADDERS

Thermal conductivity integral models have often been used to predict the thermal conductivity of silicon, including bulk silicon [24, 25], nanoscale thin films [17], and periodically porous silicon films [11]. These models consider the impact of the phonon dispersion relations, as well as mode- and wave vector–dependent phonon relaxation times, in order to compute the thermal conductivity. Specifically, the thermal conductivity can be computed from a Callaway-Holland-type model [26]:

$$k = \frac{1}{6\pi^2}\sum_j \int_q C_j(q,T)\, v_j(q)^2\, \tau_j(q,T) q^2 dq$$

$$= \frac{1}{6\pi^2}\sum_j \int_q \frac{\hbar^2 \omega_j(q)^2}{k_B T^2} \frac{\exp\left(\frac{\hbar\omega_j(q)}{k_B T}\right)}{\left(\exp\left(\frac{\hbar\omega_j(q)}{k_B T}\right)-1\right)^2} v_j(q)^2\, \tau_j(q,T)\, q^2 dq, \quad (3)$$

where k_B is the Boltzmann constant, $h = 2\pi\hbar$ is Planck's constant, and $C_j(q,T)$, $\omega_j(q)$, $v_j(q)$, and $\tau_j(q,T)$ are the specific heat, angular frequency, velocity, and relaxation time, respectively, of the phonons in branch j with wave vector q at temperature T. We first consider the dispersion relation and scattering times for bulk silicon and then include the impact of nanobeam boundary and pore boundary scattering. Finally, we estimate the impact modifying the phonon dispersion relation with a phonon bandgap.

Model for Bulk Silicon

The three acoustic branches (one longitudinal and two transverse) were considered in calculating the thermal conductivity of silicon. Though it is possible to generate the dispersion relations for silicon through both simulations [26, 27] and experiments [28], simplifying the dispersion relationship to an analytical form allows for rapid calculations of thermal conductivity. Debye models are often used in calculations but approximate the phonon velocity as constant [17]. Born-von Karman (sine-type) models more accurately represent the band structure, and the required parameters from the model can be estimated from the speed of sound and atomic density of solids [29]. In this article, we use a fourth-order polynomial fit to the longitudinal and transverse dispersion relationships in the [1,0,0] direction calculated by Weber [27] using lattice dynamics as used previously by Hopkins et al. [5].

The relaxation time of phonons in bulk silicon, $\tau_{j,\text{bulk}}(q)$, is calculated with Matthiessen's rule considering Umklapp, impurity, and boundary scattering:

$$\frac{1}{\tau_{j,\text{bulk}}(q)} = \frac{1}{\tau_{j,\text{Umklapp}}} + \frac{1}{\tau_{j,\text{impurity}}} + \frac{1}{\tau_{j,\text{boundary}}}, \quad (4)$$

where $\tau^{-1}_{j,\text{Umklapp}} = BT\omega_j(q)^2 \exp\left(-C/T\right)$, $\tau^{-1}_{j,\text{impurity}} = A\omega_j(q)^4$, and $\tau^{-1}_{j,\text{boundary}} = v_j(q)/E$, where A, B, C, and E are fitting parameters determined by fitting to data [5, 30]. In this article, the values $A = 1.32 \times 10^{-45}$ s^{-3}, $B = 1.4 \times 10^{-19}$ s/K, $C = 152$ K, and $E = 2.3 \times 10^{-3}$ m were taken from Hopkins et al. [5, 30]. At low temperatures, if the boundary scattering term is neglected, the thermal conductivity continues to increase with decreasing temperature. Above 100 K, the predicted curves of bulk silicon conductivity are independent of the choice of the fitting parameter E. Figure 3 shows the thermal conductivity calculated by this model for bulk silicon.

Nanobeam Boundary Scattering

For nanostructured silicon, boundary scattering is important, even at room temperature, and modifications to the thermal conductivity integral are required. One method is to

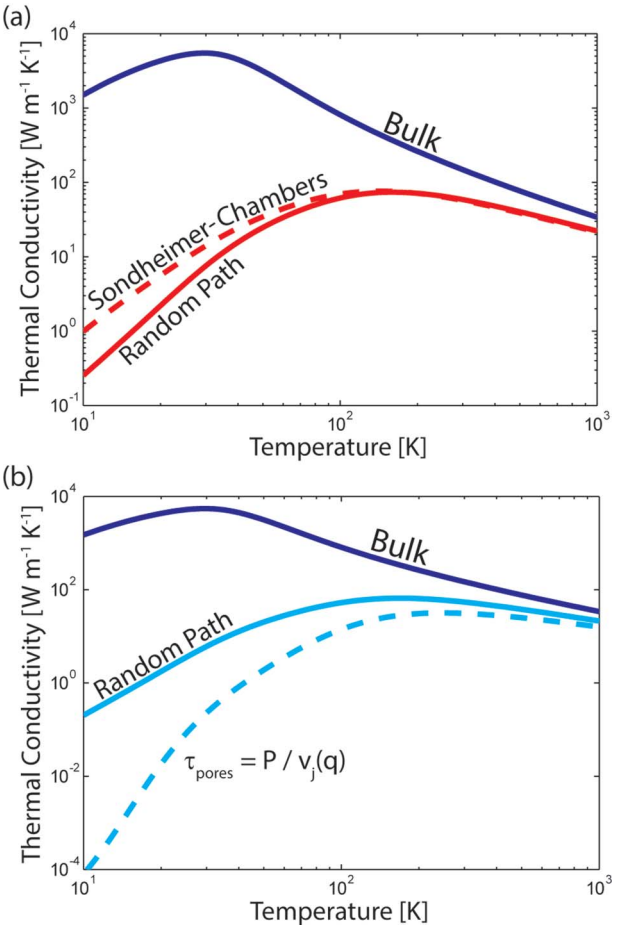

Figure 3 Calculated silicon thermal conductivity. (a) Comparison of bulk (blue line) and nanobeam (red lines) thermal conductivity. The estimated thermal conductivity for a rectangular nanobeam with a 550 nm × 200 nm cross section calculated using the Sondheimer-Chambers [32, 33] approach is shown with the dashed red line and from the random phonon path calculation with the solid red line. (b) Comparison of bulk (blue line) and nanoladder (cyan lines) thermal conductivity. For 550 nm × 200 nm nanoladders with 200-nm pores spaced by 400 nm, the dashed cyan line shows the estimation from $\tau_{pores} = P/v_j(q)$, and the solid cyan line shows the estimation from the random phonon path calculation. In both cases, the reduction due to the outer nanobeam boundaries is calculated with the random phonon path calculation method (color figure available online).

include boundary scattering in the relaxation time using Matthiessen's rule. For cylindrical nanowires, the reduced mean free path considering the nanoscale geometry can be approximated because the nanowire diameter and the mean free path is related to the scattering rate by $\Lambda_j = v_j\,(q)\,\tau_j$. Similar geometric estimates of the reduced mean free path can be made for noncylindrical nanobeams and thin films [31].

A second method for modeling the impact of boundary scattering takes into account the spectral dependence of boundary scattering and allows determination of the reduced relaxation time in more complex geometries. The bulk relaxation time is reduced by a conductivity reduction function F through

$$\tau_{j,r} = F\tau_{j,\text{bulk}}. \tag{5}$$

Expressions for the conductivity reduction function for thin wires and films have previously been derived using kinetic theory by Sondheimer [32] and Chambers [33]. Although originally derived considering electron transport, this approach is also applicable to phonon transport. Given a nanobeam with an arbitrary cross section U, a phonon originating at point O on that cross section, traveling in the polar direction (θ, ϕ), will scatter on the boundary at some point P after traveling a distance $\overline{OP}$. The conductivity reduction function for a given mean free path Λ can be calculated by integrating across the entire cross section and all polar directions [32, 33]:

$$F(U, \Lambda) = 1 - \frac{3}{4\pi U} \int_U \int_0^{2\pi} \int_0^{\pi} \sin\phi \cos^2\phi \exp\left(-\overline{OP}/\Lambda\right) d\phi d\theta dU. \tag{6}$$

For a rectangular cross section, a single set of reduction functions valid for a range of cross sections can be found by nondimensionalizing the nanobeam dimensions (the reduced thickness $\delta = H/\Lambda$ and the aspect ratio $AR = W/H$). Equation (6) is valid for purely diffuse scattering at the nanobeam boundary, but modifications are possible to account for specular reflections:

$$F(U, \Lambda, p) = (1-p)^2 \sum_{n=1}^{\infty} np^{n-1} F\left(U, \Lambda/n\right), \tag{7}$$

where p is the fraction of phonons reflected specularly from the boundaries [32, 33]. The reduction function computed from Eqs. (6) and (7) for a rectangular nanobeam with an AR = 2.75 is shown in Figure 4a for purely diffuse scattering ($p = 0$), as well as partially specular ($p = 0.3$ and $p = 0.9$). The thermal conductivity calculated with the purely diffusive reduction function for this nanobeam geometry is shown in Figure 3a.

One drawback of the Sondheimer-Chambers [32, 33] method for calculating the reduction function is the time required to complete the numerical integration with sufficient accuracy, especially for noncircular nanobeams. Specifically, because many subdivisions of the cross section and phonon propagation direction are required for accurate numerical integration, it takes several hours to generate the reduction function for a single aspect ratio. We developed a rapid method of calculating the reduction in thermal conductivity by considering the propagation of a large number of phonons starting from a random selection of points in the cross section and with a randomized propagation direction. Similar to the boundary integral approach, we computed the distance that phonons travel before scattering at a boundary. Instead of integrating across all possible start locations and propagation directions, we computed the average distance traveled by a large number of phonons with randomized start locations and propagation directions. This technique is similar to the method of McGaughey [34] and McGaughey and Jain [35] but fully incorporates the calculated boundary scattering reduction function with the thermal conductivity integral to estimate the reduction in thermal conductivity. More details on this method can be found in Appendix B.

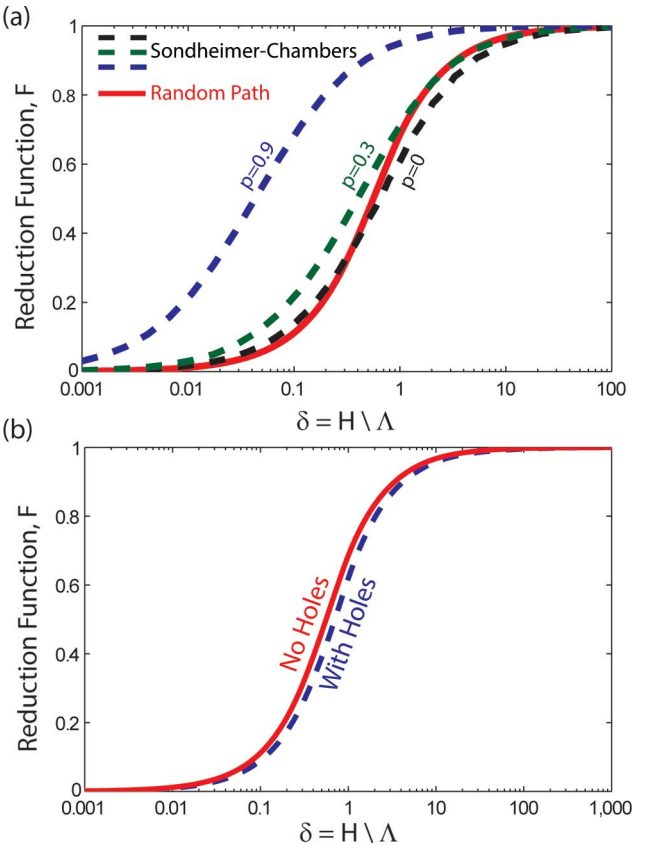

Figure 4 Conductivity reduction function. (a) Thermal conductivity reduction function for a rectangular nanobeam with AR $= W/H$ of 2.75 (no holes) following the technique of Sondheimer [32] and Chambers [33] using numerical integration (dashed lines) compared to that using the random phonon path calculation (solid line). For the Sondheimer-Chambers approach, three specularities are considered: $p = 0$ (fully diffuse), $p = 0.3$, and $p = 0.9$ (mostly specular). (b) Thermal conductivity reduction for nanoladders (blue dashed line) with AR $= 2.75$, $W/D = 2.75$, and $S/D = 2$ using the random phonon path calculation compared to that of a nanobeam without holes (AR $= 2.75$) (solid red line) (color figure available online).

The conductivity reduction function computed for a nanobeam with an aspect ratio of 2.75 is shown in Figure 4a. Considering 8,000 phonon paths for each step in 2,500 discretizations of δ, this calculation takes approximately one second to complete, which is significantly faster than the boundary integral method. In comparison to the Sondheimer-Chambers [32, 33] integral approach, the reduction function from the randomized path approach has a sharper roll-off with decreasing δ. The random path tracing method is purely geometrical, with a sharp selection between the intrinsic mean free path and the boundary scattering distance for each phonon path considered. In contrast, the Sondheimer-Chambers integral includes additional terms stemming from kinetic theory. After computing the reduction function for a range of reduced thicknesses, the thermal conductivity integral was computed and Figure 3a shows the thermal conductivity calculated using this expression.

Using the random path tracing method, the impact of boundary scattering is directly evident in the fraction of phonons scattering due to bulk processes compared to those scattering at boundaries. For a nanobeam with an aspect ratio of 2.75, Figure 5a compares

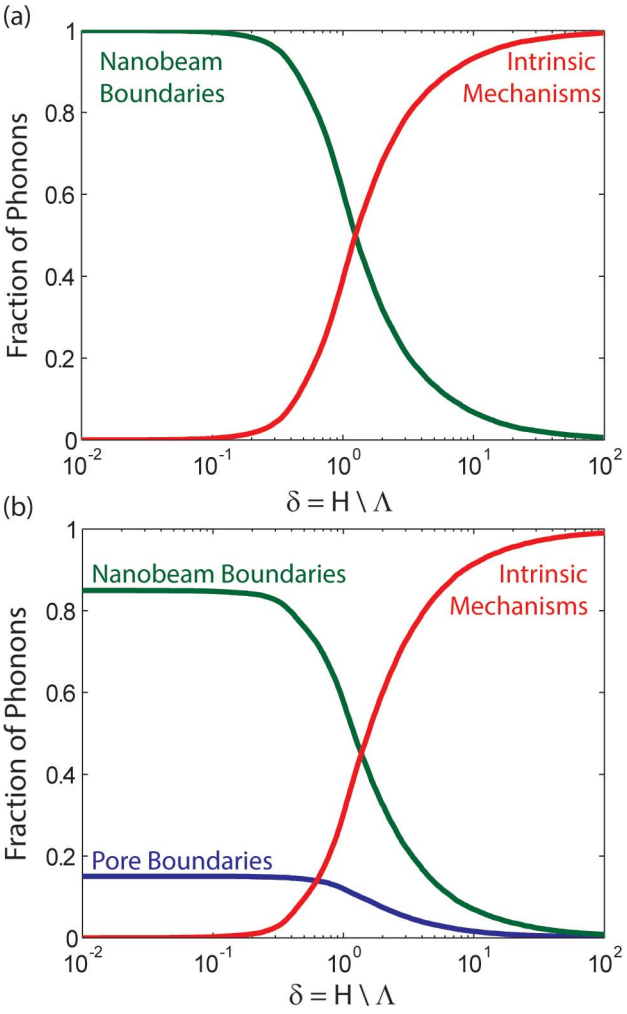

Figure 5 (a) Fraction of phonons scattered by boundaries (green) compared to intrinsic scattering mechanisms (red) for a nanobeam with AR = 2.75. (b) Fraction of phonons scattered by pores (blue) and external nanobeam boundaries (green) compared to intrinsic scattering mechanisms (red) for a nanoladder with AR = 2.75, W/D = 2.75, and S/D =2 (color figure available online).

the effect of bulk scattering processes to boundary scattering for a range of reduced thicknesses. As expected, when the reduced thickness was on the order of unity, the boundary scattering and intrinsic scattering processes contributed approximately equally. Note that when $\delta = 1$ ($\Lambda = H$), more than half the phonons scattered on boundaries before traveling their full mean path (H) and the reduction function was larger than 0.5 due to the continuum of distances traveled before scattering at the wall.

Pore Boundary Scattering

Beyond scattering at external nanobeam boundaries, in these nanoladder devices, the scattering at the pore boundaries played an important role in the thermal conductivity.

As with the nanobeam boundaries this scattering can be included either using Matthiessen's rule or through a conductivity reduction function. For microporous and nanoporous solids, Hopkins and colleagues [30] considered a boundary scattering term

$$\tau_{\text{pores}} = \frac{P}{v_j(q)}, \tag{8}$$

where P is the limiting dimension in the nanostructure, which for the two-dimensional periodically porous structures is the distance between pore boundaries ($P = S - D$). For the case of the nanoladders, the limiting dimension was the smaller of the distance between the pores and the distance between the pore edge and the side wall of the nanobeam: $P = \min\left(S - D, \frac{W-D}{2}\right)$. However, in this work, we separately account for the nanobeam boundary scattering using the conductivity reduction function described in the previous section. Thus, to determine the impact of pore scattering alone when using Eq. (8), the limiting dimension considered is $P = S - D$. Figure 3b shows the reduced thermal conductivity using this approach for a nanoladder with cross section of 550×200 nm^2, $D = 200$ nm, and $S = 400$ nm.

The random mean free path approach lends itself particularly well for calculating the reduction in the mean free path due to pore scattering. A similar algorithm to that used for the nanobeam boundary scattering calculation above was used to compute the reduction function for pore scattering in the nanoladders. More details on this method can be found in Appendix B. As illustrated by the conductivity reduction functions in Figure 4b, the presence of these pores reduces the phonon scattering time only slightly more than the nonporous nanobeams of the same cross section.

Many phonons never encounter a pore, instead scattering at external nanobeam boundaries or due to bulk processes. The relative impact of scattering processes is evident in Figure 5b from the fraction of phonons scattering due to bulk processes compared to those scattering at nanobeam boundaries and at hole boundaries. At most only ~15% of the phonons scatter on the pore boundaries for this geometry (AR = 2.75, $W/D = 2.75$, and $S/D = 2$). Thus, the thermal conductivity predicted with this method is larger than predicted by using Eq. (8), as illustrated in Figure 3b. The scattering term $\tau_{\text{pores}} = P/v_j(q)$ limits the mean free path of every phonon, whereas the random path calculation considers that some phonons do not encounter pores. However, phonons near the pores may still be impacted by the pore boundary, so the two methods could be considered bounds to the thermal conductivity reduction due to pore scattering. Figure 6 shows the predicted thermal conductivity using each method for a range of hole diameters and spacings for nanoladders with a cross section of 550 nm × 200 nm.

Estimate of Impact of Modified Phonon Dispersion Relationships

Several studies have shown modifications to the phonon band structure, specifically the opening of phononic bandgaps, in phononic crystals consisting of a two-dimensional array of air holes in a thin film [36, 37]. Recent experimental and theoretical work has suggested that these coherent phonon effects reduce the thermal conductivity [5, 11, 15, 26, 38]. For ~20-nm-thick silicon membranes with 11- and 16-nm-diameter air holes spaced by 34 nm, Yu et al. [15] measured a significant reduction in the thermal conductivity, which they attributed to coherent phonon effects. For a 500-nm-thick silicon membranes with periodic arrays of air holes with diameters on the order of several hundred nanometers, Hopkins

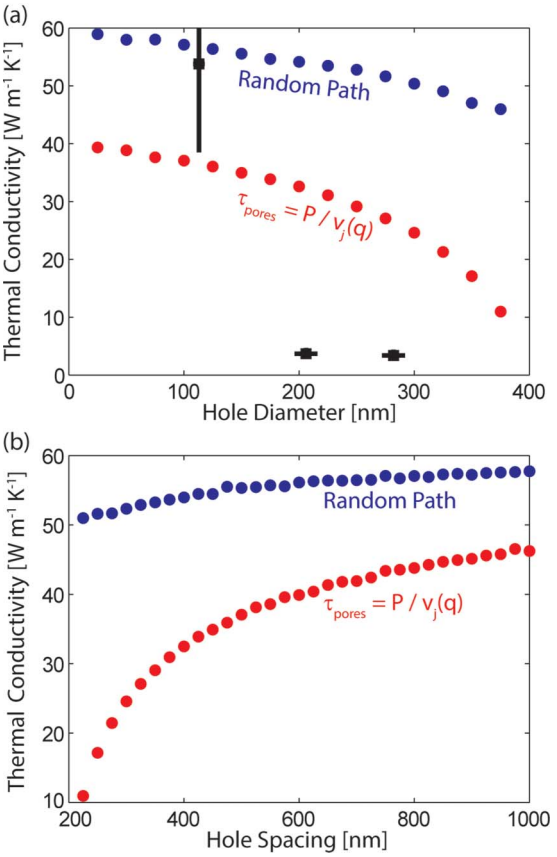

Figure 6 Impact of hole (a) diameter and (b) spacing on the thermal conductivity of 550 nm × 200 nm silicon nanoladders. In panel (a) the pore spacing is fixed at 400 nm and the experimental results from this work are shown with black squares. In panel (b) the pore diameter is fixed at 200 nm. Calculations using the random pore scattering model are shown in blue, and those using the model $\tau_{\text{pores}} = P/v_j(q)$ are shown in red (color figure available online).

et al. [5] found that to match their model of thermal conductivity to the measured values, the phonon density of states had to be altered (in addition to including scattering effects). The nanoladder design studied in this article is essentially a one-dimensional analog to the two-dimensional phononic crystal slabs.

The frequency of phonons impacted by a periodic pore structure is approximately [11]

$$f_{ph} = {}^{\pi v_{\text{avg}}}\!/_{S}, \tag{9}$$

where v_{avg} is the average speed of sound in silicon. To estimate the thermal conductivity, a phonon transmission function $\Gamma(\omega(q))$ can be included in the thermal conductivity integral:

$$k = \frac{1}{6\pi^2} \sum_j \int_q \Gamma(\omega(q))\, C_j(q,T)\, v_j(q)^2\, \tau_j(q,T) q^2 dq. \tag{10}$$

Depending on the exact geometry and material properties, a select band of phonon frequencies will be blocked by the structure [38, 39]. However, to estimate the maximum possible impact of the porous structures, this work considers the extreme case that the phononic structure blocks all phonons up to f_{ph} such that the transmission function is

$$\Gamma(\omega(q)) = \begin{cases} 0 & \omega(q) \leq 2\pi f_{ph} \\ 1 & \omega(q) > 2\pi f_{ph} \end{cases}. \tag{11}$$

For 550 nm × 200 nm nanoladders with 200-nm-diameter holes spaced by 400 nm, $f_{ph} = 51.4$ GHz, and the reduction in thermal conductivity due to any coherent phonon effects is small. For this geometry, including the effect of coherent phonons leads to only very small additional reduction in thermal conductivity compared to neglecting phononic effects (see Figure 7a). The impact of coherent effects is stronger at very low temperatures (below 50 K) but is still less than 0.02% of the nanoladder thermal conductivity. As shown in Figure 7b, coherent phonon effects become more important if the nanoladder structure is

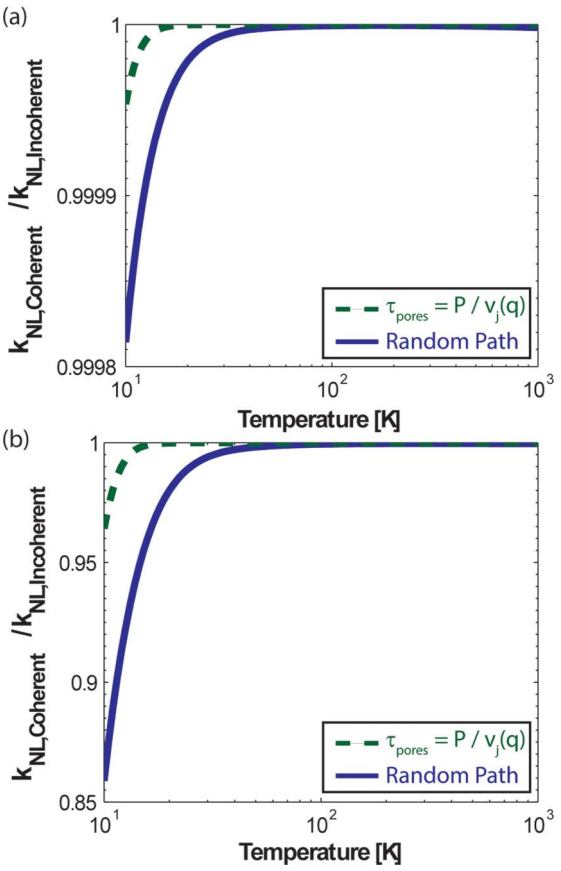

Figure 7 Ratio of the nanoladder thermal conductivity considering coherent phonon effects to that neglecting coherent phonon effects: (a) 550 nm × 200 nm, D = 200 nm, S = 400 nm; (b) 55 nm × 20 nm, D = 20 nm, S = 40 nm. Calculations using the random pore scattering model are shown with solid lines, and those using the model $\tau_{pores} = P/v_j(q)$ are shown with dashed lines (color figure available online).

fabricated an order of magnitude smaller in each dimension (55 nm × 20 nm, $D = 20$ nm, $S = 40$ nm), such that the impacted frequencies shift up to 514 GHz.

CONCLUDING REMARKS

The thermal conductivities of three porous nanoladders were measured using a steady-state electrothermal technique. The thermal conductivities were significantly reduced from bulk silicon and from the nonporous nanobeam, especially for the large-diameter pores. A Callaway-Holland model was used to compute reduction in thermal conductivity. The boundary scattering reduction function was computed both from a Sondheimer-Chambers [32, 33] approach and by tracing the paths of a large number of phonons within the nanostructure. The impact of scattering at the pore boundaries was also estimated using a random path tracing method and from the minimum pore boundary separation distance. Coherent phonon effects were considered by estimating the phonon frequencies impacted by the periodic pore structure. For these nanoladders with pores spaced by ∼400 nm, the impact of coherent effects on the thermal conductivity was negligible (<0.02% at $T < 50$ K). However, if the dimensions were reduced even by a factor of 10, coherent phonon effects were evident, especially at low temperatures (<100 K). The results of the thermal conductivity model agreed with the predicted thermal conductivity for the nanoladder with the smallest diameter pores; however, additional measurements and modeling work are needed to understand the reduction in thermal conductivity for the larger diameter pore structures. Surface roughness and nonuniformities in the pore geometry may contribute to the significantly reduced thermal conductivity for the nanoladders with large-diameter pores.

REFERENCES

1. A. Balandin, Thermal Properties of Graphene and Nanostructured Carbon Materials, *Nature Materials*, Vol. 10, pp. 569–581, 2011.
2. L.D. Hicks and M.S. Dresselhaus, Thermoelectric Figure of Merit of a One-Dimensional Conductor, *Physical Review B*, Vol. 47, pp. 16631–16634, 1993.
3. X.W. Wang, H. Lee, Y.C. Lan, G.H. Zhu, G. Joshi, D.Z. Wang, J. Yang, A.J. Muto, M.Y. Tang, J. Klatsky, S. Song, M.S. Dresselhaus, G. Chen, and Z.F. Ren, Enhanced Thermoelectric Figure of Merit in Nanostructured N-Type Silicon Germanium Bulk Alloy, *Applied Physics Letters*, Vol. 93, pp. 193121–193123, 2008.
4. J. Tang, H.-T. Wang, D.H. Lee, M. Fardy, Z. Huo, T.P. Russell, and P. Yang, Holey Silicon as an Efficient Thermoelectric Material, *Nano Letters*, Vol. 10, pp. 4279–4283, 2010.
5. P.E. Hopkins, C.M. Reinke, M.F. Su, R.H. Olsson, E.A. Shaner, Z.C. Leseman, J.R. Serrano, L.M. Phinney, and I. El-Kady, Reduction in the Thermal Conductivity of Single Crystalline Silicon by Phononic Crystal Patterning, *Nano Letters*, Vol. 11, pp. 107–112, 2010.
6. D. Song and G. Chen, Thermal Conductivity of Periodic Microporous Silicon Films, *Applied Physics Letters*, Vol. 84, pp. 687–689, 2004.
7. M. Makarova, J. Vuckovic, H. Sanda, and Y. Nishi, Two-Dimensional Porous Silicon Photonic Crystal Light Emitters, *2006 Conference on Lasers and Electro-Optics and 2006 Quantum Electronics and Laser Science Conference*, Long Beach, CA, 21–26 May 2006.
8. Y. Gong, M. Makarova, S. Yerci, R. Li, M.J. Stevens, B. Baek, S.W. Nam, R.H. Hadfield, S.N. Dorenbos, V. Zwiller, J. Vuckovic, and L. Dal Negro, Linewidth Narrowing and Purcell Enhancement in Photonic Crystal Cavitieson an Er-Doped Silicon Nitride Platform, *Optics Express*, Vol. 18, pp. 2601–2612, 2010.

9. K. Esfarjani, G. Chen, and H.T. Stokes, Heat Transport in Silicon from First-Principles Calculations, *Physical Review B*, Vol. 84, p. 085204-1–085204-11, 2011.
10. S. Benchabane, A. Khelif, W. Daniau, L. Robert, V. Petrini, B. Assouar, B. Vincent, O. Elmazria, J. Kruger, and V. Laude, Silicon Phononic Crystal for Surface Acoustic Waves, *2005 IEEE Ultrasonics Symposium*, Rotterdam, The Netherlands, 18-21 September 2005.
11. P.E. Hopkins, L.M. Phinney, P.T. Rakich, R.H. Olsson, and I. El-Kady, Phonon Considerations in the Reduction of Thermal Conductivity in Phononic Crystals, *Applied Physics A*, Vol. 103, pp. 575–579, 2010.
12. J.-H. Lee, G.A. Galli, and J.C. Grossman, Nanoporous Si as an Efficient Thermoelectric Material, *Nano Letters*, Vol. 8, pp. 3750–3754, 2008.
13. S. Mohammadi, A.A. Eftekhar, W.D. Hunt, and A. Adibi, Demonstration of Large Complete Phononic Band Gaps and Waveguiding in High-Frequency Silicon Phononic Crystal Slabs, *2008 IEEE International Frequency Control Symposium*, Honolulu, HI, 19-21 May 2008.
14. R.H. Olsson III and I. El-Kady, Microfabricated Phononic Crystal Devices and Applications, *Measurement Science and Technology*, Vol. 20, p. 012002-1–012002-13, 2009.
15. J.-K. Yu, S. Mitrovic, D. Tham, J. Varghese, and J.R. Heath, Reduction of Thermal Conductivity in Phononic Nanomesh Structures, *Nature Nanotechnology*, Vol. 5, pp. 718–721, 2010.
16. Y. Gong, B. Ellis, G. Shambat, T. Sarmiento, J.S. Harris, and J. Vuckovic, Nanobeam Photonic Crystal Cavity Quantum Dot Laser, *Optics Express*, Vol. 18, pp. 8781–8789, 2010.
17. W. Liu and M. Asheghi, Thermal Conductivity Measurements of Ultra-Thin Single Crystal Silicon Layers, *Journal of Heat Transfer*, Vol. 128, pp. 75–83, 2006.
18. W. Liu and M. Asheghi, Thermal Conduction in Ultrathin Pure and Doped Single-Crystal Silicon Layers at High Temperatures, *Journal of Applied Physics*, Vol. 98, p. 123523-1–123523-6, 2005.
19. T. Kodama, W. Park, A. Marconnet, J. Lee, M. Asheghi, and K.E. Goodson, In-Plane Thermal Conductivity Measurement on Nanoscale Conductive Materials with On-Substrate Device Configurations, *IEEE Intersociety Conference on Thermal and Thermomechanical Phenomena in Electronic Systems (ITHERM)*, San Diego, CA, 30 May-1 June 2012.
20. B. Kim, J. Nguyen, P.J. Clews, C.M. Reinke, D. Goettler, Z.C. Leseman, I. El-Kady, and R.H. Olsson, Thermal Conductivity Manipulation in Single Crystal Silicon Via Lithographycally Defined Phononic Crystals, *2012 IEEE 25th International Conference on Micro Electro Mechanical Systems (MEMS)*, Paris, France, 29 January-2 February 2012.
21. Y. He, D. Donadio, J.-H. Lee, J.C. Grossman, and G. Galli, Thermal Transport in Nanoporous Silicon: Interplay between Disorder at Mesoscopic and Atomic Scales, *ACS Nano*, Vol. 5, pp. 1839–1844, 2011.
22. A.I. Hochbaum, R. Chen, R.D. Delgado, W. Liang, E.C. Garnett, M. Najarian, A. Majumdar, and P. Yang, Enhanced Thermoelectric Performance of Rough Silicon Nanowires, *Nature*, Vol. 451, pp. 163–167, 2008.
23. G.S. Oehrlein, Dry Etching Damage of Silicon: A Review, *Materials Science and Engineering: B*, Vol. 4, pp. 441–450, 1989.
24. M.G. Holland, Analysis of Lattice Thermal Conductivity, *Physical Review*, Vol. 132, p. 2461, 1963.
25. J. Callaway, Model for Lattice Thermal Conductivity at Low Temperatures, *Physical Review*, Vol. 113, pp. 1046–1051, 1959.
26. C.M. Reinke, M.F. Su, B.L. Davis, B. Kim, M.I. Hussein, Z.C. Leseman, R.H. Olsson III, and I. El-Kady, Thermal Conductivity Prediction of Nanoscale Phononic Crystal Slabs Using a Hybrid Lattice Dynamics–Continuum Mechanics Technique, *AIP Advances*, Vol. 1, pp. 041403–041414, 2011.
27. W. Weber, Adiabatic Bond Charge Model for the Phonons in Diamond, Si, Ge, and A-Sn, *Physical Review B*, Vol. 15, pp. 4789–4803, 1977.
28. B.N. Brockhouse, Lattice Vibrations in Silicon and Germanium, *Physical Review Letters*, Vol. 2, pp. 256–258, 1959.
29. C. Dames and G. Chen, Theoretical Phonon Thermal Conductivity of Si/Ge Superlattice Nanowires, *Journal of Applied Physics*, Vol. 95, pp. 682–693, 2004.

30. P.E. Hopkins, P.T. Rakich, R.H. Olsson, I.F. El-kady, and L.M. Phinney, Origin of Reduction in Phonon Thermal Conductivity of Microporous Solids, *Applied Physics Letters*, Vol. 95, pp. 161902–161903, 2009.
31. H.B.G. Casimir, Note on the Conduction of Heat in Crystals, *Physica*, Vol. 5, pp. 495–500, 1938.
32. E.H. Sondheimer, The Mean Free Path of Electrons in Metals, *Advances in Physics*, Vol. 1, pp. 1–42, 1952.
33. R.G. Chambers, The Conductivity of Thin Wires in a Magnetic Field, *Proceedings of the Royal Society of London - Series A, Mathematical and Physical Sciences*, Vol. 202, pp. 378–394, 1950.
34. A. McGaughey, Phonon Transport in Thin Films, *7th U.S.–Japan Joint Seminar on Nanoscale Transport Phenomena—Science and Engineering*, Shima, Japan, 11-14 December 2011.
35. A.J.H. McGaughey and A. Jain, Nanostructure Thermal Conductivity Prediction by Monte Carlo Sampling of Phonon Free Paths, *Applied Physics Letters*, Vol. 100, pp. 061911–061913, 2012.
36. T. Gorishnyy, J.-H. Jang, C. Koh, and E.L. Thomas, Direct Observation of a Hypersonic Band Gap in Two-Dimensional Single Crystalline Phononic Structures, *Applied Physics Letters*, Vol. 91, pp. 121915–121913, 2007.
37. S. Mohammadi, A.A. Eftekhar, A. Khelif, W.D. Hunt, and A. Adibi, Evidence of Large High Frequency Complete Phononic Band Gaps in Silicon Phononic Crystal Plates, *Applied Physics Letters*, Vol. 92, pp. 221905–221903, 2008.
38. I. El-Kady, M.F. Su, C.M. Reinke, P.E. Hopkins, D. Goettler, Z.C. Leseman, E.A. Shaner, and R.H. Olsson III, Manipulation of Thermal Phonons: A Phononic Crystal Route to High-Zt Thermoelectrics, *Proceedings of the SPIE*, Vol. 7946, pp. 794615–794619, 2011.
39. C.M. Reinke, M.F. Su, R.H. Olsson III, and I. El-Kady, Realization of Optimal Bandgaps in Solid–Solid, Solid–Air, and Hybrid Solid–Air–Solid Phononic Crystal Slabs, *Applied Physics Letters*, Vol. 98, pp. 061912–061913, 2011.

APPENDIX A: DETAILS OF THE NUMERICAL ELECTROTHERMAL MODEL

Consider a steady-state energy balance around a differential element of the nanoladder of length Δx: $q_{\text{gen}} + q_{\text{in}} - q_{\text{out}} = 0$. The rate of heat generation in the palladium film is $q_{\text{gen}}(x,T) = \frac{I^2\rho(T)}{A_{c,m}(x)}$, where $\rho(T) = \rho_o(1 + \alpha(T - T_o))$ and $A_{c,m}(x) = H_m W(x)$ is the cross-sectional area of the metal film. The rates of heat transfer into (q_{in}) and out of (q_{out}) the differential element are due to thermal conduction in both the silicon and metal layers. Assuming a spatially uniform palladium thermal conductivity but spatially varying silicon conductivity, the energy balance becomes

$$\frac{I^2\rho(T)}{A_{c,m}(x)} + k_m \frac{\partial}{\partial x}\left(A_{c,m}(x)\frac{dT}{dx}\right) + \frac{\partial}{\partial x}\left(A_{c,s}(x)\,k_s(x)\frac{dT}{dx}\right) = 0, \tag{A1}$$

where $A_{c,s}$ is the cross-sectional area of the silicon beam. Further expansion of the differential terms leads to the differential equation:

$$\frac{I^2\rho_0\alpha}{H_m W(x)}T + \left((H_m k_m + H k_s(x))\frac{dW(x)}{dx} + H W(x)\frac{dk_s(x)}{dx}\right)\frac{dT}{dx} + (H_m k_m + H k_s(x))\,W(x)\frac{d^2T}{dx^2} = \frac{-I^2(\rho_0 - \rho_0\alpha T_0)}{H_m W(x)}, \tag{A2}$$

Figure A1 shows a schematic of the geometry considered in this model, highlighting key parameters. For the nanoladders in this work, the thermal conductivity of the silicon at the nonporous beam ends k_e was taken from the measured thermal conductivity of the

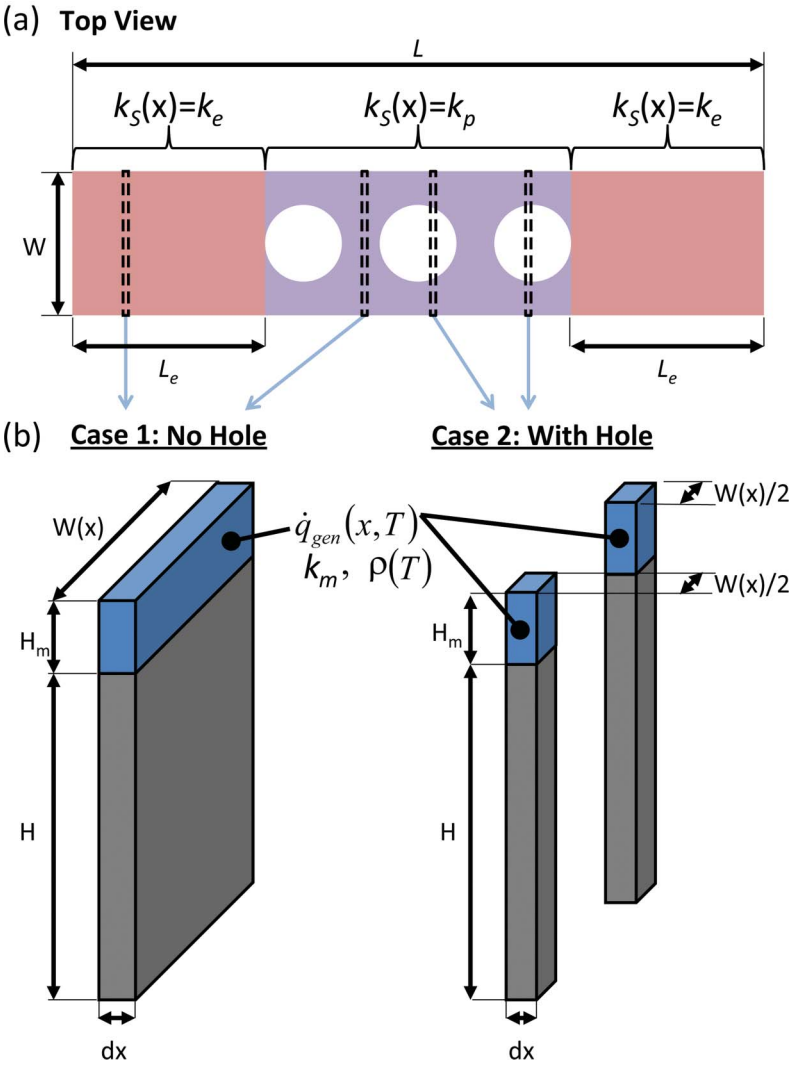

Figure A1 Schematic showing the geometry and key parameters for the numerical model of the temperature distribution in the nanobeams and nanoladders. (a) In the top view of the porous nanobeam, three regions of the beam are indicated, including two nonporous regions at the end of the beam of length L_e where $k_s(x) = k_e$ and the porous region in the center of the beam with $k_s(x) = k_p$. Four example discretized elements are shown with dashed boxes and correspond to the discretized elements shown in panel (b). The two leftmost boxes correspond to case 1 (no hole) with the discretized element spanning the full width of the nanobeam. The two rightmost elements each contain a portion of a pore, corresponding to case 2, and consist of two subelements with widths less than the full beam width (color figure available online).

nonporous nanobeam, and the thermal conductivity of the porous region k_p was assumed uniform:

$$k_s(x) = \begin{cases} k_e, \text{ where } x < L_e \\ k_p, \text{ where } L_e \le x \le L - L_e \\ k_e, \text{ where } x > L - L_e \end{cases} \tag{A3}$$

where L_e is the length of the nonporous beam ends: $L_e = \frac{L-(N_h-1)S-D}{2}$.

Using the finite difference method to expand the derivatives, we arrive at a matrix equation, $B = \mathbf{A}\mathrm{T}$, where the elements of B are

$$B_i = \frac{-I^2 \rho_o \left(1 - \alpha T_o\right)}{H_m W_i} \tag{A4}$$

and the elements of $\mathbf{A}$ are

$$A_{i,i-1} = -\left(\frac{H_m k_m + H k_{s,i}}{4\Delta x^2}\right)\left(W_{i+1} - W_{i-1}\right) + \frac{H_m k_m + H k_{s,i}}{\Delta x^2} W_i - \frac{H W_i}{4\Delta x^2}\left(k_{s,i+1} - k_{s,i-1}\right), \tag{A5}$$

$$A_{i,i} = \frac{I^2 \rho_o \alpha}{H_m W_i} - \frac{2\left(H_m k_m + H k_{s,i}\right) W_i}{\Delta x^2}, \text{and} \tag{A6}$$

$$A_{i,i+1} = \left(\frac{H_m k_m + H k_{s,i}}{4\Delta x^2}\right)\left(W_{i+1} - W_{i-1}\right) + \frac{H_m k_m + H k_{s,i}}{\Delta x^2} W_i + \frac{H W_i}{4\Delta x^2}\left(k_{s,i+1} - k_{s,i-1}\right). \tag{A7}$$

Given the beam width and thermal conductivity as a function of position, the temperature profile along the nanoladder can be found by inverting the matrix A: $\mathrm{T} = \mathbf{A^{-1}}\mathrm{B}$. The total electrical resistance of the beam is then found from summing the resistance of the differential elements of the beam $R = \sum_i \frac{\Delta x}{\rho(T_i) H_m W_i}$, accounting for the temperature-dependent resistivity. Note that for regions with holes, the beam width W_i is the total width of the silicon. In other words, at positions corresponding to the center of a hole, the width of the element is $W_i = W - D$.

APPENDIX B: DETAILS OF THE RANDOM PATH TRACING PHONON SCATTERING MODEL

For a nanobeam with an arbitrary cross section, we take the following approach to generate a reduction function analogous to that of the Sondheimer-Chambers [32, 33] approach:

1. Consider a single intrinsic mean free path E_0 (corresponding to a reduced thickness $\delta = H/\Lambda_0$).
2. Select a random phonon start position (x, y) and propagation direction (θ, φ).
3. Calculate the distance that the phonon would travel before scattering at boundary ($\overline{OP}$).
4. Calculate the mean free path of the ith phonon, Λ_i, by selecting the smaller of the distance $\overline{OP}$ and the intrinsic mean free path Λ_0.
5. Repeat steps 2–4 for many start positions and propagation directions.
6. Compute the reduction function $F\left(\delta, AR\right) = \frac{1}{N_p \Lambda_0} \sum_{i=1}^{N_p} \Lambda_i$, where N_p is the number of paths considered in step 5.
7. Repeat steps 1–6 to generate the reduction function for a range of mean free paths (reduced thicknesses).

To include the effect of pore scattering, a few modifications to the algorithm for the nanobeam are required. Specifically, phonons must be allowed to start anywhere within

an entire period of the pore structure and can scatter due to either bulk processes, pore boundary scattering, or scattering at the boundary of the nanobeam. Many pores must be considered because some of the phonons may not impact the first pore but one further down the nanoladder. The new algorithm to compute the reduction function is explained below:

1. Consider a single intrinsic mean free path Λ_0 (corresponding to a reduced thickness $\delta = H/\Lambda_0$).
2. Select a random phonon start position (x, y, z) and propagation direction (θ, φ). The start position is selected so that no phonon starts in a hole. A full unit cell of the pore geometry is considered instead of a single cross section.
3. Calculate the distance that the phonon would travel before scattering at an external nanobeam boundary ($\overline{OP}$).
4. Calculate the distance that the phonon would travel before scattering at a pore boundary ($\overline{OR}$). The propagation path of many phonons will never intersect a pore boundary, in which case $\overline{OR} = \infty$.
5. Calculate the mean free path of the ith phonon, Λ_i, by selecting the smaller of the distances: $\overline{OP}$, $\overline{OR}$, and Λ_0.
6. Repeat steps 2–5 for many start positions and propagation direction.
7. Compute the average of the mean free paths for this value of intrinsic mean free path and the reduction function $F(\delta, AR, S, D) = \frac{1}{N_p \Lambda_0} \sum_{i=1}^{N_p} \Lambda_i$, where N_p is the number of paths considered in step 6.
8. Repeat steps 1–7 to generate the reduction function for a range of mean free paths (reduced thicknesses).